

# Multi-scale Segmentation and Surface Fitting for Measuring 3D Macular Holes

Amar V. Nasrulloh, Chris G. Willcocks, Philip T. G. Jackson, Caspar Geenen, Maged S. Habib, David H. W. Steel, and Boguslaw Obara\*

**Abstract**—Macular holes are blinding conditions where a hole develops in the central part of retina, resulting in reduced central vision. The prognosis and treatment options are related to a number of variables including the macular hole size and shape. High-resolution spectral domain optical coherence tomography (SD-OCT) allows precise imaging of the macular hole geometry in three dimensions, but the measurement of these by human observers is time consuming and prone to high inter- and intra-observer variability, being characteristically measured in 2D rather than 3D. We introduce several novel techniques to automatically retrieve accurate 3D measurements of the macular hole, including: surface area, base area, base diameter, top area, top diameter, height, and minimum diameter. Specifically, we introduce a multi-scale 3D level set segmentation approach based on a state-of-the-art level set method, and we introduce novel curvature-based cutting and 3D measurement procedures. The algorithm is fully automatic, and we validate our extracted measurements both qualitatively and quantitatively, where our results show the method to be robust across a variety of scenarios. Our automated processes are considered a significant contribution for clinical applications.

**Index Terms**—Macular holes, measurement of macular holes, 3D segmentation, multi-scale techniques, level set methods, curvature-based surface fitting.

## I. INTRODUCTION

A MACULAR hole is a hole that develops in the central part of the retina, and is most commonly caused by age related vitreous traction on the central fovea [1], [2]. The condition affects approximately 2 in every 1000 individuals over the age of 40 [3], and can have a devastating impact on the quality of life and on an individual's independence [2]. Surgery offers a 90% likelihood of closing the hole but the improvement in vision depends on the duration of the hole, and is related to a number of variables including macular hole size and shape [4], [5]. Recently, [6] have proposed the first approach to segment and measure the macular hole; however

Manuscript received April 19, 2005; revised August 26, 2015. A.V.Nasrulloh is supported by Indonesian Endowment Fund for Education (LPDP Indonesia).

A.V.Nasrulloh is with School of Engineering and Computing Sciences Durham University, Durham, UK, on leave from Physics Study Program, University of Lambung Mangkurat, Banjarbaru, Indonesia. (e-mail: amar.v.nasrulloh@durham.ac.uk).

C.G.Willcocks, P.T.G.Jackson and B.Obara\* are with School of Engineering and Computing Sciences Durham University, Durham, UK (e-mail: {christopher.g.willcocks, p.t.g.jackson, boguslaw.obara}@durham.ac.uk).

C.Geenen and M.S.Habib are with Sunderland Eye Infirmary, Queen Alexandra Road, Sunderland, UK (e-mail: {Caspar.Geenen, Maged.Habib}@chsft.nhs.uk).

D.H.W.Steel is with Sunderland Eye Infirmary, Queen Alexandra Road, Sunderland, UK and Institute of Genetic Medicine, Newcastle University, Newcastle Upon Tyne, UK (e-mail: David.Steel@chsft.nhs.uk).

*Asterisk indicates corresponding author.*

their approach acquires the measurements of the 3D macular hole by combining individual 2D graph-cuts segmentations of slices in the 3D image, rather than considering the overall 3D geometry.

Our approach includes a fully 3D segmentation algorithm using a state-of-the-art level set method based on the local Gaussian distribution fitting (LGDF) energy functional [7]. However, despite the high computational expense with level sets, we achieve fast convergence without relying on high-end hardware acceleration. This is accomplished by employing a 3D multi-scale approach that exploits the fact that the macular holes are considered large objects within the 3D image, processing initial updates at lower spatial resolutions.

This is followed by a novel curvature-based surface cutting procedure, which separates the macular hole from its background, allowing for fully-automatic measurement of the shape and volume. The method is shown to be stable to the various 3D input images of different macular holes without requiring retuning of the parameters, and is shown to be more accurate than existing graph cuts segmentation approaches.

## II. CONTRIBUTIONS

The objective of this paper is to develop an automatic approach to efficiently extract precise and robust measurements of 3D macular holes. To this purpose, we have developed a level set segmentation approach that improves the efficiency of the state-of-the-art LGDF energy by considering multiple scales. Further, we have introduced a novel curvature-based surface cutting procedure to separate the segmented hole from its background, and proposed novel procedures for automatically calculating the desired measurements robustly.

Specifically, we have:

- Composed an automatic pipeline for measuring 3D macular holes.
- Introduced a 3D multi-scale active surface which is 61 times faster than the original LGDF implementation.
- Introduced an automatic and novel curvature-based surface cutting procedure to separate the 3D macular hole from the vitreous body.
- Introduced automatic and novel procedures for capturing specific macular hole measurements, based on our robust centerline definition.
- Provided quantitative and qualitative validation of the algorithm's robustness and performance across a variety of different 3D macular hole images.

### III. RELATED WORK

#### A. Retinal imaging

The problem of analysis in retinal disease is a large multidisciplinary research area with collaboration from researchers and clinicians [8], [9]. A comprehensive review by [10] shows that analysis in retinal disease has led to significant advances in preventing blindness and visual loss, using 2D digital fundus photography and 3D optical coherence tomography (OCT). The macula refers to the central part of the retina with the fovea, a specialized part of it with high photoreceptor density, sited at its centre. It is responsible for fine detailed vision including reading and facial recognition. OCT is considered a powerful technique for imaging macular disease including macular edema and macular holes [11]. In contrast, compared to macular edema, research into automatic macular hole analysis is very limited.

#### B. Macular hole imaging

Optical coherence tomography allows clinicians to characterize the shape and volume of macular holes [12], leading to new insights into the pathogenesis of macular hole formation [13]. Spectral domain optical coherence tomography (SD-OCT) provides higher resolution images with reduced artefacts compared to time domain OCT [2]. Recently, [14] propose a length-adaptive graph search metric that accurately segments the retina/vitreous boundary of a 2D OCT image, whereas [15] use auto-thresholding in ImageJ [16] and measure the binary segmentation of the forward-facing view of a macular hole.

To calculate the volume of a macular hole, [17] propose fitting a truncated cone to a 2D view of the macular hole, which fails to capture irregularities and depth information. Alternative 3D methods apply 2D segmentation algorithms to each slice in the 3D geometry [6] and then accumulate the results to provide analysis of macular hole's 3D shape and volume, however the slice-by-slice approach requires verification by a human operator to confirm the segmentation at each slice. The minimum diameter measurement is also calculated based on single 2D slice [6], [18], which may fail to consider profiles that are elliptical in cross-section.

Similarly, [19] distinguish normal macula and multiple macular pathologies which are macular edema, macular hole, and age-related macular degeneration from the foveal slices in retinal OCT images on a slice-by-slice basis. They employ a simple edge-based technique with a canny edge-detector, which has known limitations where edges are weak, blurred and/or broken, however they apply a multi-scale spatial pyramid and identify local binary patterns in texture and shape encoding to efficiently infer geometric features at multiple scales and spatial resolutions.

In contrast to these approaches, 3D level set methods are able to enforce continuity along all three axes with subpixel accuracy and smooth surfaces, while remaining robust to noise. They can segment objects with weak, broken and/or distorted edges by not relying on image gradients [20].

#### C. Active contours

The snakes active contour model, first introduced by [21], is widely used in the image segmentation field to deform an initial

curve to lock onto edges, lines and endpoints interactively. This concept was extended by [22], who considered the contour neighbourhood as a region-based energy. Malladi et al. in [23] formulated the energy update rule using level sets, which allows a deformable implicitly defined region to surround or fill inside the object of interest. By introducing a curvature term [24], the evolving speed of the deformable region (contour or surface) can be controlled such as to prevent leaking through small gaps in the object boundary allowing for segmentation of more complex shapes.

The Mumford-Shah energy functional [25], establishes an optimal partitioning scheme to divide an image into parts, which are piecewise-smooth within segments. Early active contour models solved the Mumford-Shah under the assumption that segments had piece-wise constant intensity [20], which was later addressed by [26] who define a pixel's energy based on its local neighborhood within a predetermined scale rather than the mean intensity of an entire segment. [7] improves on this by modifying the data fitting term to consider the intensity variance, through a *maximum a posteriori probability* formulation based on Gaussian approximation of the intensity distribution, called the local Gaussian distribution fitting (LGDF) energy. The LGDF energy functional is considered a state-of-the-art in the active contour segmentation literature, however it has currently only been applied to small 2D images due to its high computational requirements, in particular relying on multiple Gaussian convolutions per update iteration.

Further, it is difficult for standard segmentation approaches to automatically separate the macular hole from the vitreous body. Previous work individually applies a 2D graph cuts algorithm to each 3D slice of the macular hole, where the graph cut boundaries are specified with morphological erosions of adjacent slices. However this approach requires manual verification of each slice by a human operator to check the segmentation is plausible [6]. We perform a fully automatic 3D segmentation algorithm with an automatic procedure to cut the relevant volume of the hole from the background vitreous body in order to obtain the required measurements.

### IV. MATERIALS

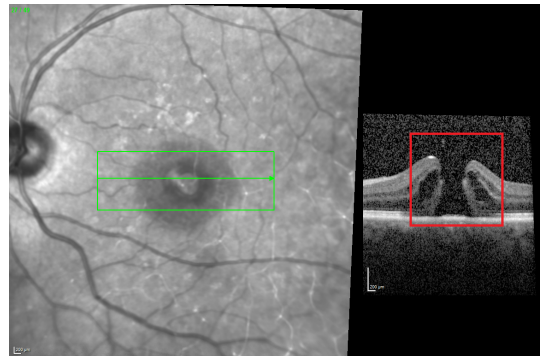


Fig. 1. 2D view of a 3D SD-OCT image of the retina (left) and its 2D cross-section along the green arrowed line. The region of interest is marked by the red box (right). Scale bar: X = 11.58 [ $\mu\text{m}$ ] and Y = 3.87 [ $\mu\text{m}$ ].

In this paper, we used 30 images of macular hole cases that were provided by the Sunderland Eye Infirmary, Sunderland,

UK. Patients underwent spectral domain optical coherence tomography (SD-OCT) on the Heidelberg Spectralis (Heidelberg Engineering, Frankfurt, USA) immediately preoperatively as part of routine care. A high density central horizontal scanning protocol with 30 micrometers line spacing was used in the central 10 by 15 degrees. All scans used a 25 automatic real time (ART) setting enabling multisampling and noise reduction over 25 images. The images were exported anonymised and in a non-compressed format. All of our input images are  $200 \times 200 \times 49$  voxel sub-regions of the raw data, chosen such that the macular hole is in the centre (see Fig. 1).

## V. METHOD

We present a novel segmentation approach based on level set methods and regression analysis, for extracting specific measurements of the 3D shape and volume of the macular hole. The proposed approach consists of three main parts, discussed in subsections V-B-C, V-D and V-E respectively.

### A. Overview

Level set segmentation methods, including the LGDF energy functional in [7], implicitly define the boundary of a segmentation region as the zero level set of a scalar field  $\phi(\vec{x})$ . That is, the interior of the region is defined as  $\{\vec{x} : \phi(\vec{x}) < 0\}$ , with  $\phi(\vec{x}) = 0$  on the boundary. Given an input image  $I$ ,  $\phi$  is iteratively deformed using variational methods so as to minimise the energy functional  $E(\phi, I)$ , resulting in a smooth boundary that separates regions of different properties.

The initial value of  $\phi$  is set automatically as a small spherical seed region  $\phi(\vec{x}) = |\vec{x} - \vec{x}_0| - r$ , where  $\vec{x}_0$  is  $(0.5, 0.6, 0.5)$  in normalized image coordinates, slightly below the midpoint of the image, so as to be close to the base of the macular hole (Fig. 2a). This is then clamped with a binary step function using a constant value  $c = 2$  outside the sphere and  $c = -2$  inside the sphere. The segmentation process involves iteratively updating  $\phi$  so as to minimise the LGDF functional  $E^{\text{LGDF}}(\phi, I)$  yielding an implicit boundary between vitreous humor and retina tissues (Fig. 2b-c)

To increase performance, we initially segment the cavity at low-resolution, then when convergence is met we progressively upscale both  $\phi$  and  $I$  and iterate until  $\phi$  and  $I$  are at their original resolution and fully converged (Fig. 2b-d). We then cut the segmented cavity from its opening in a separate procedure (Fig. 2e) before extracting the final measurements.

### B. 3D Local Gaussian Distribution Fitting (LGDF) Energy

We adopt the LGDF energy functional in [7] (originally implemented in 2D) for a 3D active surface. The total energy  $\mathcal{E}(\phi)$  is given by the summation of three terms: energy  $E^{\text{LGDF}}(\phi, I)$  which drives the contour to fit along salient image edges, a length term  $\mathcal{L}(\phi)$  which penalizes the length of the contour to ensure smoothness, and a regularization term  $\mathcal{P}(\phi)$  which keeps  $\phi$  approximating a signed distance function to ensure numerical stability:

$$\mathcal{E}(\phi, I) = \alpha E^{\text{LGDF}}(\phi, I) + \nu \mathcal{L}(\phi) + \mu \mathcal{P}(\phi) \quad (1)$$

where  $\alpha, \nu, \mu > 0$  are weighting constants.  $E^{\text{LGDF}}(\phi, I)$  is the sum of the energy of each voxel  $E^{\text{LGDF}}(\phi, I, \vec{x})$ :

$$\begin{aligned} E^{\text{LGDF}}(\phi, I, \vec{x}) = & - \int_{\Omega} \omega(\vec{y} - \vec{x}) \log(p_{1,\vec{x}}(I(\vec{y}))) M_1(\phi(\vec{y})) d\vec{y} \\ & - \int_{\Omega} \omega(\vec{y} - \vec{x}) \log(p_{2,\vec{x}}(I(\vec{y}))) M_2(\phi(\vec{y})) d\vec{y} \end{aligned} \quad (2)$$

where  $\omega(\vec{x} - \vec{y})$  is a Gaussian weighting function centered on  $\vec{x}$ ,  $p_{1,\vec{x}}$  and  $p_{2,\vec{x}}$  are the likelihoods assigned to the pixel intensities by Gaussian models of the intensity distributions inside and outside the contour, and  $M_1$  and  $M_2$  are indicator functions separating the regions inside and outside the contour. This is further elaborated in [7].  $\mathcal{P}(\phi)$  penalizes the deviation of  $\phi$  from signed distance function [26]:

$$\mathcal{P}(\phi) = \int \frac{1}{2} (|\nabla \phi(\vec{x})| - 1)^2 d\vec{x} \quad (3)$$

and  $\mathcal{L}(\phi)$  penalizes the length of the contour [27] for a smooth surface:

$$\mathcal{L}(\phi) = \int |\nabla H(\phi(\vec{x}))| d\vec{x} \quad (4)$$

where  $\vec{x} = [x, y, z]$  is a voxel in an image  $I$ .  $H$  is a Heaviside function which we discretize by:

$$H(x) = \frac{1}{2} \left[ 1 + \frac{2}{\pi} \arctan(x) \right] \quad (5)$$

The energy  $E^{\text{LGDF}}(\phi, I)$  is able to segment objects with inhomogenous local intensity mean  $u(\vec{x})$  and variance  $\sigma(\vec{x})^2$  (Eq.s 22-23 in [7]) allowing for slow changes in intensity across an object but penalizing sudden changes within it. The image force term is calculated for both inside and outside the contour  $i = 1, 2$  respectively, by applying the calculus of variations [7], yielding:

$$e_i(\vec{x}) = \int_{\Omega} \omega(\vec{y} - \vec{x}) \left[ \log(\sigma_i(\vec{y})) + \frac{(u_i(\vec{y}) - I(\vec{x}))^2}{2\sigma_i(\vec{y})^2} \right] d\vec{y} \quad (6)$$

This local energy is applied locally with the delta function  $\delta(x)$  (derivative of Eq. 5)  $-\delta(\phi)(e_1 - \lambda e_2)$  with a weighting parameter  $\lambda > 1$  to give preference to external force  $e_2$  and hence the contour is preferable to grow to fill the hole cavity. The functional can then be minimized by solving the gradient descent flow equation [7] which yields the following update rule:

$$\frac{\partial \phi}{\partial t} = -\alpha \delta(\phi)(e_1 - \lambda e_2) + \nu \delta(\phi) \kappa + \mu (\nabla^2 \phi - \kappa) \quad (7)$$

where  $\kappa$  is the curvature [24]:

$$\kappa = \text{div} \left( \frac{\nabla \phi}{|\nabla \phi|} \right) \quad (8)$$

To segment the image, we iteratively update the level set function  $\phi$  according to Eq. 7. However this is computationally expensive, especially in the case of 3D OCT images requiring tens of thousands of iterations before convergence.

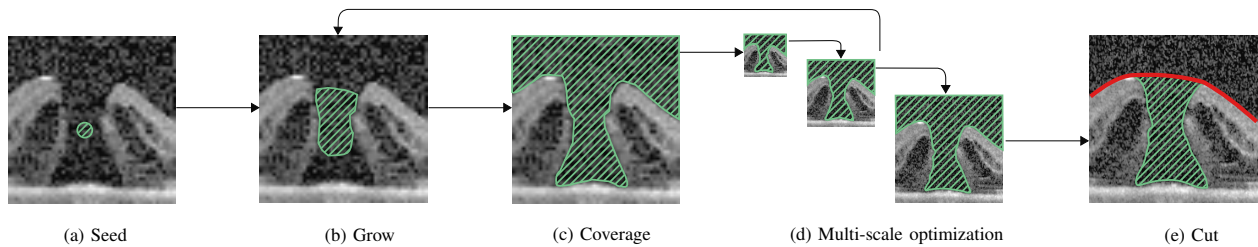


Fig. 2. The proposed 3D multi-scale approach iteratively deforms an initial region (a) to fill (b-c) the cavity of the hole at low-resolution, and then progressively upscales (d) and reiterates until convergence. This is followed by a curvature-based cutting procedure (e).

### C. 3D Multi-scale LGDF

We improve performance by initially segmenting the hole cavity at a small scale, by downsampling  $I$  and  $\phi$  (Fig. 3a). Solving Eq. 7 at this small scale converges much more quickly and captures the overall shape of the macular hole. However the zero-crossing  $\phi = 0$  lacks the finer high-frequency surface details. Therefore we progressively upscale  $\phi$  and re-solve Eq. 7, for multiple scale levels:

$$S = \{\vec{s}_i\}, \forall i \in [1, n], \vec{s}_i < \vec{s}_{i+1} \quad (9)$$

where  $\vec{s}_i = (s_x, s_y, s_z)$  and  $s_x, s_y, s_z$  are scaling factors for each the  $x, y, z$  image dimensions accordingly. Solving Eq. 7 for these subsequent scales now only takes a small number of iterations given that  $\phi = 0$  is already near the object boundary in each case (Fig. 3b). Finally we are able to process  $\phi$  at the original resolution ( $\vec{s}_n = (1, 1, 1)$ ) with a small number of iterations, capturing the finer surface details (Fig. 3c).

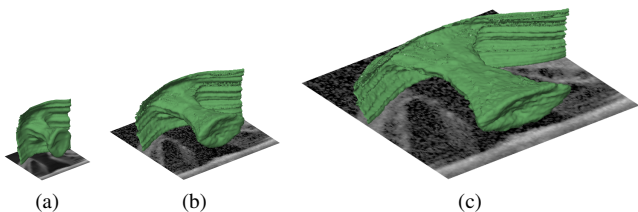


Fig. 3. Result of 3D macular hole based on our multi-scale level set segmentation approach. In our experiment, we choose  $n = 3$  scale levels with scale parameters: (a)  $\vec{s}_1 = (0.25, 0.25, 1)$ , (b)  $\vec{s}_2 = (0.5, 0.5, 1)$ , (c)  $\vec{s}_3 = (1, 1, 1)$ . We do not alter the  $z$ -dimension in our case, as it is already shallow in the original OCT input images.

Downscaling  $\phi$  and  $I$  for the initial multi-scale stage  $\vec{s}_1$  is able to segment the macular hole, exploiting the fact that the hole is a large object in the OCT image. However noise introduced by OCT propagates through the downsampled  $I$ , which may prevent the initial evolution from evolving to fill the hole cavity. Therefore we denoise the  $I$  for the smallest scale  $\vec{s}_1$  using a Wiener filter by [28], [29], which is effective at removing the speckle noise encountered in OCT imaging [30], and the result is shown in Fig. 4a. In subsequent scales  $\vec{s}_i$  where  $2 \leq i \leq n$ , we do not denoise the image as (1) we assume the contour is already filling the hole cavity at this stage, and (2) we wish to capture the finer surface details unhindered by the denoising process.

Implementation of  $E^{\text{LGDF}}$  in 3D requires  $6 \times 3\text{D}$  Gaussian convolutions per iteration, required for calculating intermediate

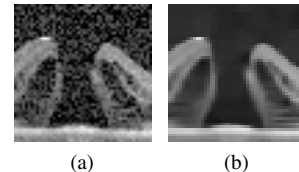


Fig. 4. (a) OCT image from red box in Fig. 1 downsampled by  $\vec{s}_1 = (0.25, 0.25, 1)$ , (b) Result of denoising using the Wiener filter with default parameters [28], [29].

variables in Eq. 6. These convolutions are a performance bottleneck, therefore we use an optimized implementation of Gaussian convolution in the Fourier domain [31] which supports arbitrarily large standard deviation  $\sigma$  without impacting the performance.

### D. Curvature-based cutting surface

The problem of LGDF is that it will only separate the vitreous humour from the retinal tissue, and cannot separate the macular hole from the main body of vitreous humour. We need to cut the previously segmented vitreous humour in such a way as to only capture the macular hole shape (Fig. 2e). In our approach, we initially attempted to cut the macular hole based on intensity information in the image, but we found that a curvature-based approach is more robust across the different images.

We compute curvature  $\kappa$  of the 3D active surface by using an efficient integral invariant approach [32], [33] based on [34], which uses a spherical kernel in 3D. We apply the signum function to  $\phi$  and then convolve with a spherical kernel of radius  $r$  (Fig. 5a). This effectively computes the difference between the inside and outside volume within a sphere centered at every point on the surface. The radius of the kernel determines the scale of the curves that it responds strongly to. In our case we find that  $r = 116.10 \mu\text{m}$  captures the lip of the macular hole (in  $200 \times 200 \times 49$  [voxels] OCT images), while smoothing out high-frequency surface noise.

The curvature  $\kappa$  (Fig. 5b) is defined over all points in the OCT image, however we are only interested in the surface curvature at the lip of the macular hole. We therefore binarize  $\phi$  and select only the surface voxels where  $\kappa < 0$  (brown voxels in Fig. 5c). We then fit a two variable 2<sup>nd</sup> order polynomial to these voxels (Fig. 5d). In some pathological cases (e.g. Image 25, Table III), the curvature based cutting surface is too high,

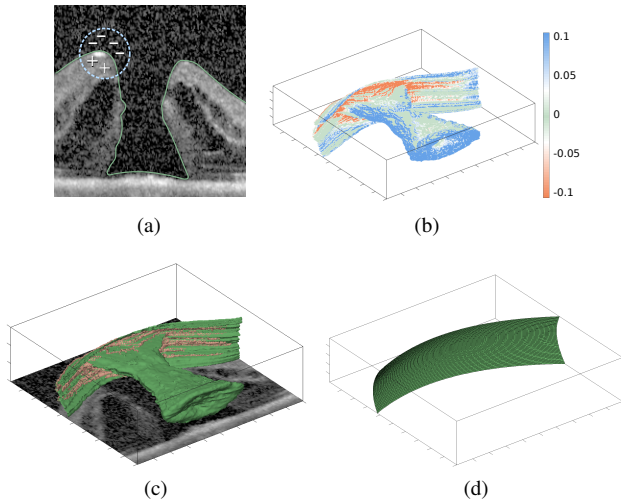


Fig. 5. (a) Spherical kernel applied at the surface  $\phi = 0$ , (b) Curvature  $\kappa$  on the 3D surface, (c) Surface voxels with negative  $\kappa$  (brown), (d) Fitting a  $2^{nd}$  order polynomial to these voxels.

and does not cleanly separate the macular hole. Therefore, we translate the surface down by a fixed amount (we choose  $154.80 \mu m$ ), and then “re-grow” the macular hole up to a fixed distance (we choose  $100.62 \mu m$ ) on all images. We find that these extra steps increase our overall accuracy.

### E. Measurements

From a 2D side-view of the 3D macular hole, ophthalmologists require precise measurements of the minimum diameter (most narrow point on the hole) and base diameter. To compute these measurements robustly, we first extract a smooth ‘centerline’ of the macular hole, denoted  $C = \{\vec{c}_i\}$ , to act as a frame of reference for our measurements (Fig. 6 red dashed line). The centerline is calculated using the approach proposed in [35], but extended to 3D. Specifically, each coordinate of the ‘centerline’ is defined to be the centroid of the slice:

$$\vec{c}_i = \left( \int_{\Psi_i} \vec{x} d\vec{x} \right) / \left( \int_{\Psi_i} d\vec{x} \right) = \frac{1}{|\Psi_i|} \sum_{\vec{x} \in \Psi_i} \vec{x} \quad (10)$$

where  $\Psi_i \subset \Omega \subset \mathbb{R}^2$  is a set of the binary segmented pixels for the  $i^{th}$  slice (in the y-axis) in the macular hole after the cutting procedure. The centerline is then smoothed using robust local regression [36], as in the paper [35], using a smoothing parameter (in our case we choose 0.9 to represent a span of 90% of the signal). This is important as it ensures the centerline acts as a descriptor for the overall shape and direction of the hole (especially in the middle as we are not concerned about the centerline veering off at the top and base of the hole) and ensures that it remains highly insensitive to surface noise.

We compute the height measurement of the macular hole as the length of  $C$ , and then take the normal of the middle point along  $C$  (shown by purple and yellow arrows in Fig. 6 left) to act as a basis for the three planes (Fig. 6 middle: pink, blue, and green lines). The remaining measurements (top area, base area, and smallest area) are inferred from these planes: by examining the cross-section at distances 20% and 80% along the curve, and then finding the minimal cross-sectional

area between these two planes accordingly. Since these cross-sections are generally elliptical, rather than circular, we define their diameters as their major axis lengths, as in [6].

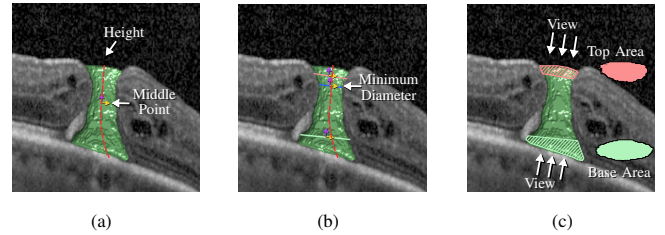


Fig. 6. (a) We initially compute a smooth centerline (dashed red line), (b) normal at the central point is used as a basis for finding the top region and bottom region, as well as the minimal diameter between these two regions, (c) we view orthogonal projections of the cropped 3D volumes (striped regions) separately from above and below, giving us 2D areas (opaque regions) measuring the top and bottom of the hole accordingly.

Ophthalmologists currently use the minimum diameter from a 2D side view of the macular hole. Therefore we first find the smallest cross-sectional area between the top and bottom planes, and then calculate the diameter from this cross-section’s centroid to act in place of the 2D measurement.

### F. Method parameters and suggested default values

We found stable default level set evolution parameters through both our own empirical tuning across 30 images provided by the Sunderland Eye Infirmary, Sunderland, UK, and also through an experiment by minimizing the mean Jaccard Index across the 30 images with ground-truth segmentations using the built-in MATLAB genetic algorithm implementation [37]. We found that the results of the genetic algorithm coincide with our own findings, whereby the default values are chosen to be:  $\sigma = 4$ ,  $\alpha = 20$ ,  $\mu = 1$ ,  $\nu = 39$ ,  $\lambda = 1.04$ , across all images. We conducted a cross-validation experiment to evaluate the robustness of these suggested parameter values ( $\sigma$ ,  $\alpha$ ,  $\mu$ ,  $\nu$ , and  $\lambda$ ) using leave-one-out validation [38] (suitable for such small datasets). The leave-one-out cross-validation across all 30 images results in a mean Jaccard Index of 0.9644 and standard deviation 0.0015. The small standard deviation values indicate the stability of our proposed parameters.

## VI. RESULTS AND DISCUSSION

### A. Qualitative Validation

In this section, we present the results of our automatic segmentation approach for 30 real-world OCT images provided by the Sunderland Eye Infirmary, Sunderland, UK. Tables I to III show the results of our multi-scale 3D segmentation after the curvature cutting procedure for each patient, and also a 2D z-slice showing the maximal hole cross-section of the 3D segmented hole. The results demonstrate that our approach is able to successfully capture the macular hole in all the images, in particular several challenging cases such as the narrow hole in Image 8 and the complex scenario in Image 12. Furthermore, our curvature-based cutting procedure is robust and can correctly identify the lip of holes that are valley-shaped (Image 2, Image 25), hill-shaped (Image 1, Image 8, Image 14, ...), flat (Image 6, Image 7, Image 16), and slanted (Image 9).

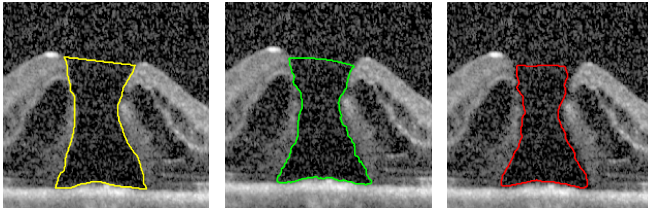
The curvature cutting procedure is excluded for Image 30 as the hole is fully enclosed and without any opening (Table III).

*B. Quantitative Validation*

In order to validate our method quantitatively, we compare the shape of our automatically segmented macular hole with 3D ground truth segmentations. These ground truth segmentations were acquired by a clinical eye surgeon manually sketching a 2D region for each slice of the macular hole for 10 images (Table I). The results in Table V show the accuracy, sensitivity, Jaccard index (ratio of intersection and union between our segmentation and ground truth) and the Dice similarity coefficient (DSC), as defined in [39], [40]. These metrics are calculated (1) between the 3D ground truth sketched region, (2) for the same dataset of our 3D multi-scale LGDF (MS-LGDF) segmentation, (3) for a 3D continuous max-flow (CMF) graph cuts [41]–[43] based approach using a  $5 \times 5 \times 5$  [voxels] 3D median filter pre-processing as with [6]. Table V also show a side-by-side comparison with the ground truth, our method, and the existing approach in Fig. 7. In general, we see that our method scores highly in all cases and that our method more closely captures the shape of the macular hole, in particular at the macular hole boundary.

TABLE V  
VALIDATION OF MACULAR HOLE SEGMENTATION RESULTS  
(MEAN ± STANDARD DEVIATION) WITH THE GROUND TRUTH BETWEEN  
MS-LGDF AND 3D CMF

Segmentation Method	Accuracy %	Sensitivity %	Jaccard Index %	DSC %
MS-LGDF	99.19 ± 00.56	85.18 ± 04.63	76.34 ± 10.31	86.19 ± 07.55
CMF	98.83 ± 00.74	71.89 ± 07.61	66.31 ± 10.51	79.27 ± 08.33



(a) Ground truth (b) MS-LGDF approach (c) CMF approach

Fig. 7. 2D cross-sections comparing macular hole segmentations with the ground truth by an expert, our method, and a 3D CMF graph-cuts approach.

We show the 3D measurements extracted with our approach in Table IV. Pixels are converted to  $[mm]$  metric scaling according to the OCT image metadata, yielding the real size and form of the macular hole (volume, surface area, base area, base diameter, top area, top diameter, height, and minimum diameter). The Bland and Altman method [44], [45] was used to calculate the mean difference ( $\bar{d}$ ) and standard error ( $se$ ) for the base diameter (BD) and minimum diameter (MD). This includes 30 datasets (Table VI) and ground truths acquired from the average of two manual measurements, taken by a clinical eye surgeon at 4 month intervals (intra-observer validation). The validation between the ground truth and MS-LGDF has smaller difference than validation between the ground truth and CMF.

TABLE I  
SEGMENTATION RESULTS

	3D Segmentation	2D Cross-Section
Image 1		
Image 2		
Image 3		
Image 4		
Image 5		
Image 6		
Image 7		
Image 8		
Image 9		
Image 10		

TABLE II  
SEGMENTATION RESULTS

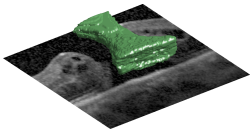
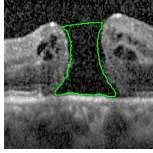
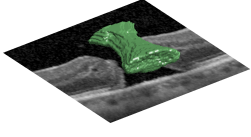
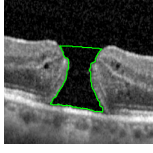
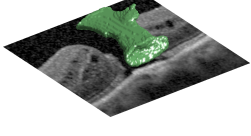
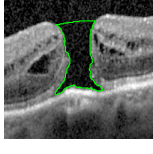
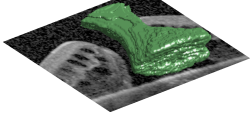
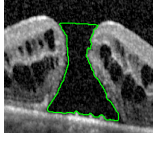
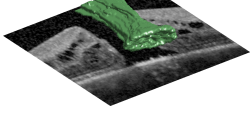

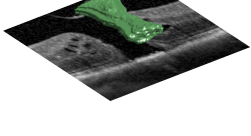

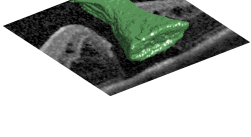

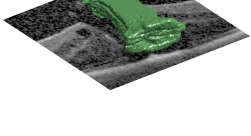

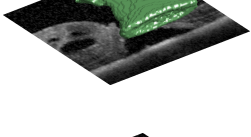

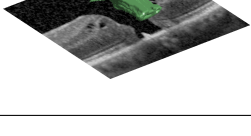

	3D Segmentation	2D Cross-Section
Image 11		
Image 12		
Image 13		
Image 14		
Image 15		
Image 16		
Image 17		
Image 18		
Image 19		
Image 20		

TABLE III  
SEGMENTATION RESULTS

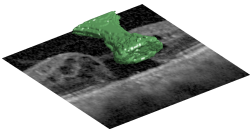
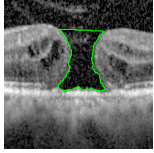
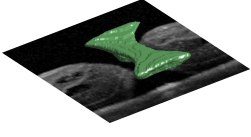

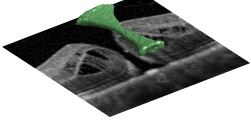

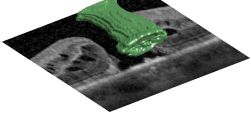
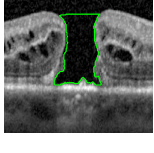
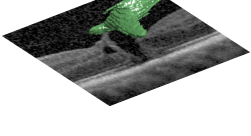
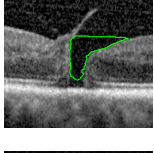
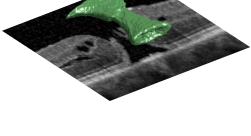

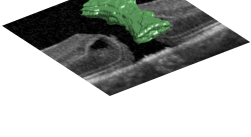
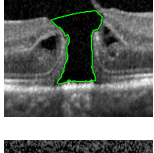
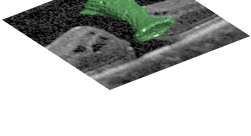
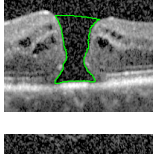
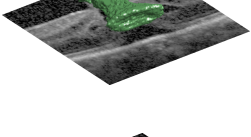
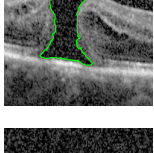
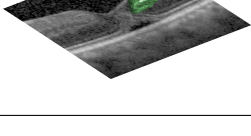
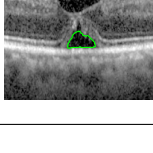
	3D Segmentation	2D Cross-Section
Image 21		
Image 22		
Image 23		
Image 24		
Image 25		
Image 26		
Image 27		
Image 28		
Image 29		
Image 30		

TABLE IV  
MEASUREMENTS OF MACULAR HOLES

3D Image Data	Volume [ $10^{-3}mm^3$ ]	Surface Area [ $mm^2$ ]	Base Area [ $mm^2$ ]	Base Diameter [ $mm$ ]	Top Area [ $mm^2$ ]	Top Diameter [ $mm$ ]	Height [ $mm$ ]	Minimum Diameter [ $mm$ ]
Image 1	148.55	2.72	0.266	0.97	0.141	0.69	1.43	0.46
Image 2	85.45	1.61	0.199	0.83	0.153	0.56	0.50	0.52
Image 3	82.63	1.73	0.164	0.70	0.128	0.66	0.98	0.46
Image 4	57.94	1.48	0.145	0.71	0.122	0.62	1.06	0.24
Image 5	95.95	1.97	0.219	0.86	0.118	0.65	1.27	0.39
Image 6	45.33	1.19	0.123	0.66	0.065	0.50	0.95	0.34
Image 7	20.25	0.79	0.036	0.34	0.073	0.52	0.97	0.13
Image 8	66.43	1.50	0.164	0.73	0.092	0.55	1.27	0.20
Image 9	61.99	1.35	0.175	0.74	0.098	0.55	0.92	0.31
Image 10	49.36	1.31	0.124	0.70	0.058	0.49	1.21	0.31
Image 11	99.61	2.12	0.247	0.92	0.109	0.69	1.11	0.39
Image 12	62.04	1.41	0.156	0.73	0.103	0.59	1.03	0.34
Image 13	59.46	1.54	0.108	0.54	0.107	0.73	1.19	0.34
Image 14	187.48	3.36	0.374	1.26	0.125	0.67	1.52	0.43
Image 15	76.86	1.90	0.147	0.74	0.092	0.56	1.27	0.44
Image 16	48.72	1.26	0.067	0.49	0.096	0.58	1.08	0.32
Image 17	135.13	2.61	0.253	0.90	0.093	0.63	1.47	0.40
Image 18	54.84	1.29	0.239	1.05	0.086	0.63	0.63	0.52
Image 19	110.10	1.89	0.221	0.64	0.166	0.52	1.12	0.32
Image 20	41.62	1.13	0.036	0.34	0.123	0.62	0.97	0.35
Image 21	64.17	1.58	0.163	0.84	0.121	0.63	0.95	0.31
Image 22	25.95	0.77	0.087	0.37	0.102	0.53	0.58	0.20
Image 23	24.11	0.83	0.043	0.39	0.091	0.56	1.18	0.15
Image 24	65.96	1.67	0.135	0.72	0.089	0.52	1.07	0.39
Image 25	38.80	1.07	0.011	0.20	0.265	1.10	0.70	0.20
Image 26	53.74	1.35	0.091	0.55	0.140	0.58	1.11	0.23
Image 27	59.82	1.43	0.085	0.52	0.138	0.69	1.07	0.28
Image 28	51.59	1.34	0.107	0.63	0.125	0.64	1.07	0.25
Image 29	56.02	1.44	0.160	0.73	0.085	0.52	1.03	0.35
Image 30	7.25	0.26	0.056	0.47	0.011	0.22	0.26	0.22

MS-LGDF is shown to be robust and stable, producing the same results when run on the same data. The Bland and Altman plots in Fig. 8 - Fig. 10 from Table VI show the agreement between the manual clinician measurements, our approach, and the graph cuts approach. The intraclass correlations two-way model Case 2, ICC(A,1) [46], was calculated to show correlation of intra-observer, manual - MS-LGDF, and manual - CMF (Table VI). The correlation coefficient shows greater agreement between clinician measurements and our approach than with the CMF method. It is worth noting that the manual 2D measurements are fundamentally limited by their assumption that the cross-section of the macular hole is circular. This assumption fails in cases where the cross-sections are elliptical. Therefore we expect to see some disagreement between the proposed automated 3D measurement, which is not limited to such cases, and the manual measurements.

C. Performance

In our experiments, we measure the performance for all input OCT images with size  $200 \times 200 \times 49$  [voxels] at all the stages in our approach. In particular, the average segmentation

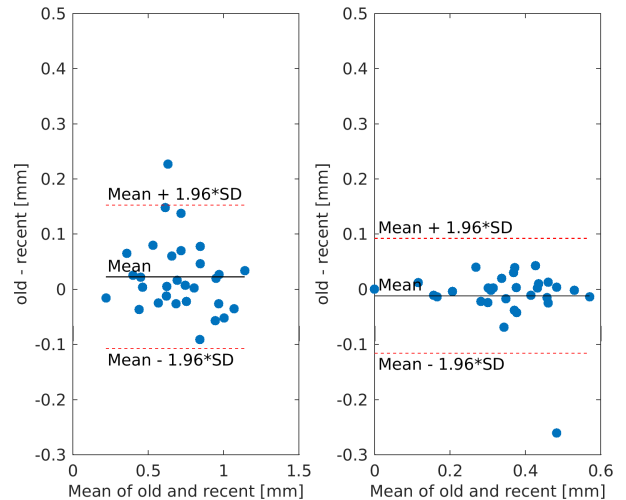


Fig. 8. Bland-Altman plot of base diameter (left) and minimum diameter (right) for intra-observer from Table VI.



TABLE VI

VALIDATION OF THE BASE DIAMETER (BD) AND MINIMUM DIAMETER (MD). FOR INTRA-OBSERVER COMPARISON,  $\bar{d}$  IS THE OLD MEASUREMENT MINUS THE RECENT. OTHERWISE,  $\bar{d}$  IS THE MANUAL MEASUREMENT MINUS OUR APPROACH OR THE GRAPH CUTS APPROACH.

Observer		$\bar{d}$ [mm]	se [mm]	Confidence [mm]	ICC
Intra-Observer	BD	0.023	0.012	0.025	0.9539
	MD	-0.012	0.010	0.020	0.9153
Manual-MS-LGDF	BD	0.033	0.018	0.036	0.9032
	MD	0.023	0.014	0.028	0.7849
Manual-CMF	BD	0.105	0.020	0.041	0.7744
	MD	0.040	0.015	0.031	0.6778

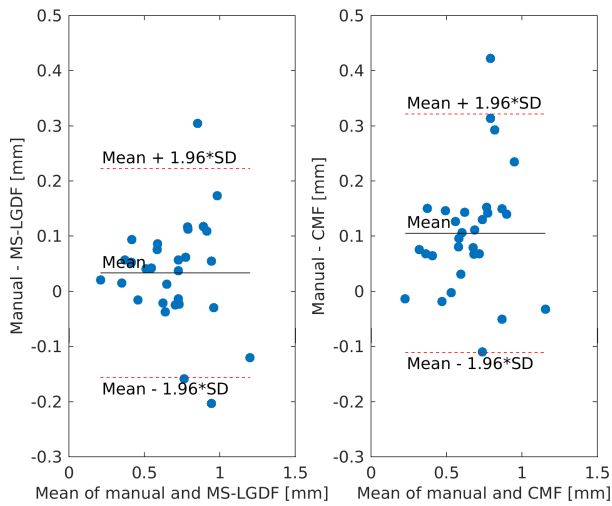


Fig. 9. Bland-Altman plot of base diameter for the manual measurement minus our approach (left) and the graph cuts approach (right) from Table VI.

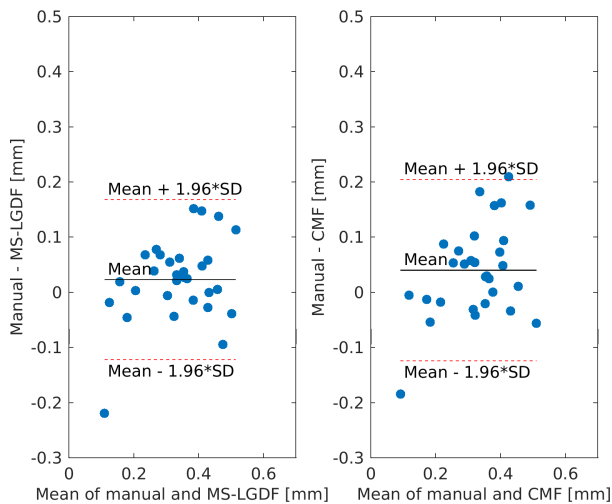


Fig. 10. Bland-Altman plot of minimum diameter for the manual measurement minus our approach (left) and the graph cuts approach (right) from Table VI.

performance of our 3D MS-LGDF is 147.65 seconds (2.46 minutes), which is significantly faster than the original 3D LGDF with a mean of 9122.87 seconds (2.5 hours) to converge. The mean time for the surface cutting procedure is 19.84 seconds. While the timings in our unoptimized MATLAB CPU implementation are considered acceptable, we believe our method can be heavily optimized if rewritten in C/C++. Additionally, the average segmentation performance of our MATLAB GPU-Array [37] implementation is 91.70 seconds for 3D MS-LGDF and 11.45 seconds for the surface cutting procedure (significantly faster than manual segmentation, which take 28.10 minutes in average).

The mean time for our automatic procedures to acquire all of the measurements is 1.15 minutes per OCT image, which is largely due to calculating volumetric analysis metrics in Table IV such as volume, surface area, base area, base diameter, top area, top diameter, height and minimum diameter. The automatic minimum diameter calculation takes the longest time due to finding the minimal cross-sectional area between 20% and 80% of these two planes. The average times to measure base diameter and minimum diameter manually are 19.06 seconds and 22.73 seconds respectively (total for both is 41.79 seconds). This exclude calculating the areas, compared to 1.15 minutes for calculating all the measurement using our unoptimized automatic method.

VII. CONCLUSION AND FUTURE WORK

In conclusion, we have proposed an automatic and robust method to both segment and extract measurements from 3D OCT images of macular holes. In particular, we found that the lip or opening of the macular hole can be automatically cut based on curvature information, and that a significant performance increase can be obtained over state-of-the-art level set methods for large objects through multi-scale techniques. Furthermore, we have proposed a novel method to collect various macular hole measurements through our definition of a robust centerline, and the method has been validated both quantitatively and qualitatively.

In the future, we would like to extend our approach to automatically extract more recent measurements, such as the area ratio factor (ARF) shown to be an effective predictive factor for diagnostic and treatment outcomes [47].

REFERENCES

- [1] W. E. Smiddy and H. W. Flynn, "Pathogenesis of macular holes and therapeutic implications," *American Journal of Ophthalmology*, vol. 137, no. 3, pp. 525–537, 2004.
- [2] D. Steel and A. Lotery, "Idiopathic vitreomacular traction and macular hole: a comprehensive review of pathophysiology, diagnosis, and treatment," *Eye*, vol. 27, pp. S1–S21, 2013.
- [3] S. S. Thapa, R. Thapa, I. Paudyal, S. Khanal, J. Aujla, G. Paudyal, and G. van Rens, "Prevalence and pattern of vitreo-retinal diseases in nepal: the bhaktapur glaucoma study," *BMC ophthalmology*, vol. 13, no. 1, p. 9, 2013.
- [4] H. A. Madi, I. Masri, and D. H. Steel, "Optimal management of idiopathic macular holes," *Clinical Ophthalmology*, vol. 10, pp. 97–116, 2016.
- [5] D. H. W. Steel, C. Parkes, V. T. Papastavrou, P. J. Avery, I. A. El-Ghrably, M. S. Habib, M. T. Sandinha, J. Smith, K. P. Stannard, D. Vaideanu-Collins, and R. J. Hillier, "Predicting macular hole closure with ocriplasmin based on spectral domain optical coherence tomography," *Eye*, vol. 30, pp. 740–745, 2016.

- [6] D. Xu, A. Yuan, P. K. Kaiser, S. K. Srivastava, R. P. Singh, J. E. Sears, D. F. Martin, and J. P. Ehlers, "A novel segmentation algorithm for volumetric analysis of macular hole boundaries identified with optical coherence tomography," *Investigative Ophthalmology & Visual Science*, vol. 54, no. 1, pp. 163–169, 2013.
- [7] L. Wang, L. He, A. Mishra, and C. Li, "Active contours driven by local Gaussian distribution fitting energy," *Signal Processing*, vol. 89, no. 12, pp. 2435–2447, 2009.
- [8] M. D. Mul, A. D. Bont, and M. Berg, "IT-supported skill-mix change and standardisation in integrated eyecare: lessons from two screening projects in The Netherlands," *International Journal of Integrated Care*, vol. 7, no. 2, pp. 1–10, 2007.
- [9] A. G. Marrugo, M. S. Millán, G. Cristóbal, S. Gabarda, M. Sorel, and F. Sroubek, "Image analysis in modern ophthalmology: from acquisition to computer assisted diagnosis and telemedicine," in *SPIE Optics, Photonics, and Digital Technologies for Multimedia Applications II*, Brussels, Belgium, 1 June 2012, p. 84360C.
- [10] M. D. Abramoff, M. K. Garvin, and M. Sonka, "Retinal imaging and image analysis," *IEEE Reviews in Biomedical Engineering*, vol. 3, pp. 169–208, 2010.
- [11] C. A. Puliafito, M. R. Hee, C. P. Lin, E. Reichel, J. S. Schuman, J. S. Duker, J. A. Izatt, E. A. Swanson, and J. G. Fujimoto, "Imaging of macular diseases with optical coherence tomography," *Ophthalmology*, vol. 102, no. 2, pp. 217–229, 1995.
- [12] M. R. Hee, C. A. Puliafito, C. Wong, J. S. Duker, E. Reichel, J. S. Schuman, E. A. Swanson, and J. G. Fujimoto, "Optical coherence tomography of macular holes," *Ophthalmology*, vol. 102, no. 5, pp. 748–756, 1995.
- [13] A. Gaudric, B. Haouchine, P. Massin, M. Paques, P. Blain, and A. Erginay, "Macular hole formation: new data provided by optical coherence tomography," *Archives of Ophthalmology*, vol. 117, no. 6, pp. 744–751, 1999.
- [14] B. Keller, D. Cunefare, D. S. Grewal, T. H. Mahmoud, J. A. Izatt, and S. Farsiu, "Length-adaptive graph search for automatic segmentation of pathological features in optical coherence tomography images," *Journal of Biomedical Optics*, vol. 21, no. 7, pp. 076015–076015, 2016.
- [15] A. Shahlace, E. Rahimy, J. Hsu, O. P. Gupta, and A. C. Ho, "Preoperative and postoperative features of macular holes on en face imaging and optical coherence tomography angiography," *Eye*, vol. 30, pp. 740–745, 2016.
- [16] C. A. Schneider, W. S. Rasband, and K. W. Eliceiri, "Nih image to imagej: 25 years of image analysis," *Nature Methods*, vol. 9, no. 7, pp. 671–675, 2012.
- [17] T. Ozturk, E. Karahan, D. Er, M. Kaya, N. Kocak, and S. Kaynak, "Effect of macular hole volume on postoperative central macular thickness," *Arquivos Brasileiros de Oftalmologia*, vol. 79, no. 3, pp. 137–142, 2016.
- [18] Y. Teng, M. Yu, Y. Wang, X. Liu, Q. You, and W. Liu, "OCT angiography quantifying choriocapillary circulation in idiopathic macular hole before and after surgery," *Graefes' Archive for Clinical and Experimental Ophthalmology*, vol. 255, pp. 893–902, 2017.
- [19] Y.-Y. Liu, M. Chen, H. Ishikawa, G. Wollstein, J. S. Schuman, and J. M. Rehg, "Automated macular pathology diagnosis in retinal OCT images using multi-scale spatial pyramid and local binary patterns in texture and shape encoding," *Medical Image Analysis*, vol. 15, no. 5, pp. 748–759, 2011.
- [20] T. F. Chan and L. A. Vese, "Active contours without edges," *IEEE Transactions on Image Processing*, vol. 10, no. 2, pp. 266–277, 2001.
- [21] M. Kass, A. Witkin, and D. Terzopoulos, "Snakes: Active contour models," *International Journal of Computer Vision*, vol. 1, no. 4, pp. 321–331, 1988.
- [22] R. Ronfard, "Region based strategies for active contour models," *International Journal of Computer Vision*, vol. 13, no. 2, pp. 229–251, 1994.
- [23] R. Malladi, J. A. Sethian, and B. C. Vemuri, "Shape modeling with front propagation: A level set approach," *IEEE Transactions on Pattern Analysis and Machine Intelligence*, vol. 17, pp. 158–175, 1995.
- [24] S. Osher and J. A. Sethian, "Fronts propagating with curvature-dependent speed: algorithms based on Hamilton-Jacobi formulations," *Journal of Computational Physics*, vol. 79, no. 1, pp. 12–49, 1988.
- [25] D. Mumford and J. Shah, "Optimal approximations by piecewise smooth functions and associated variational problems," *Communications on Pure and Applied Mathematics*, vol. 42, no. 5, pp. 577–685, 1989.
- [26] C. Li, C.-Y. Kao, J. C. Gore, and Z. Ding, "Minimization of region-scalable fitting energy for image segmentation," *IEEE Transactions on Image Processing*, vol. 17, no. 10, pp. 1940–1949, 2008.
- [27] C. Li, C. Xu, C. Gui, and M. D. Fox, "Level set evolution without re-initialization: a new variational formulation," in *Conference on Computer Vision and Pattern Recognition*, vol. 1, Washington DC, USA, 20–25 June 2005, pp. 430–436.
- [28] M. Maggioni and A. Foi, "Nonlocal transform-domain denoising of volumetric data with groupwise adaptive variance estimation," in *IS&T/SPIE Electronic Imaging, Computational Imaging X*, California, USA, 9 February 2012, p. 82960O.
- [29] M. Maggioni, V. Katkovnik, K. Egiazarian, and A. Foi, "Nonlocal transform-domain filter for volumetric data denoising and reconstruction," *IEEE Transactions on Image Processing*, vol. 22, no. 1, pp. 119–133, 2013.
- [30] A. Ozcan, A. Bilenca, A. E. Desjardins, B. E. Bouma, and G. J. Tearney, "Speckle reduction in optical coherence tomography images using digital filtering," *Journal of the Optical Society of America A*, vol. 24, no. 7, pp. 1901–1910, 2007.
- [31] M. W. Law and A. Chung, "Efficient implementation for spherical flux computation and its application to vascular segmentation," *IEEE Transactions on Image Processing*, vol. 18, no. 3, pp. 596–612, 2009.
- [32] D. Coeurjolly, J.-O. Lachaud, and J. Levallois, "Implementation of integral based digital curvature estimators in DGtal," *Imagen-A*, vol. 3, pp. 27–31, 2013.
- [33] —, "Integral based curvature estimators in digital geometry," in *International Conference on Discrete Geometry for Computer Imagery*, Seville, Spain, 20–22 March 2013, pp. 215–227.
- [34] H. Pottmann, J. Wallner, Q.-X. Huang, and Y.-L. Yang, "Integral invariants for robust geometry processing," *Computer Aided Geometric Design*, vol. 26, no. 1, pp. 37–60, 2009.
- [35] C. G. Willcocks, P. T. G. Jackson, C. J. Nelson, and B. Obara, "Extracting 3D parametric curves from 2D images of helical objects," *IEEE Transactions on Pattern Analysis and Machine Intelligence*, , forthcoming.
- [36] W. S. Cleveland, "Robust locally weighted regression and smoothing scatterplots," *Journal of the American Statistical Association*, vol. 74, no. 368, pp. 829–836, 1979.
- [37] MATLAB, *version 8.6 (R2015b)*. Natick, Massachusetts: The MathWorks Inc., 2015.
- [38] R. Kohavi, "A study of cross-validation and bootstrap for accuracy estimation and model selection," in *International Joint Conference on Artificial Intelligence*, Montreal, Quebec, Canada, 20–25 August 1995, pp. 1137–1145.
- [39] A. Ahirwar, "Study of techniques used for medical image segmentation and computation of statistical test for region classification of brain MRI," *International Journal of Information Technology and Computer Science*, vol. 5, no. 5, pp. 44–53, 2013.
- [40] A. A. Taha and A. Hanbury, "Metrics for evaluating 3D medical image segmentation: analysis, selection, and tool," *BMC Medical Imaging*, vol. 15, no. 1, p. 29, 2015.
- [41] J. Yuan, C. Schörr, and G. Steidl, "Simultaneous higher-order optical flow estimation and decomposition," *SIAM Journal on Scientific Computing*, vol. 29, no. 6, pp. 2283–2304, 2007.
- [42] J. Yuan, E. Bae, and X.-C. Tai, "A study on continuous max-flow and min-cut approaches," in *Computer Vision and Pattern Recognition*, San Francisco, USA, 13–18 June 2010, pp. 2217–2224.
- [43] J. Yuan, E. Bae, X.-C. Tai, and Y. Boykov, "A continuous max-flow approach to Potts model," in *European Conference on Computer Vision*, Crete, Greece, 5–11 September 2010, pp. 379–392.
- [44] J. M. Bland and D. G. Altman, "Statistical methods for assessing agreement between two methods of clinical measurement," *Lancet*, vol. 327, no. 8476, pp. 307–310, 1986.
- [45] D. Giavarina, "Understanding Bland Altman analysis," *Biochemia Medica*, vol. 25, no. 2, pp. 141–151, 2015.
- [46] K. O. McGraw and S. P. Wong, "Forming inferences about some intraclass correlation coefficients," *Psychological Methods*, vol. 1, no. 1, pp. 30–46, 1996.
- [47] X.-Y. Geng, H.-Q. Wu, J.-H. Jiang, K. Jiang, J. Zhu, Y. Xu, J.-C. Dong, and Z.-Z. Yan, "Area and volume ratios for prediction of visual outcome in idiopathic macular hole," *International Journal of Ophthalmology*, vol. 10, no. 8, pp. 1255–1260, 2017.